Journal of Materials Chemistry A

ROYAL SOCIETY OF CHEMISTRY

PAPER

View Article Online
View Journal | View Issue



Cite this: J. Mater. Chem. A, 2024, 12, 25359

# Covalent organic framework-based Li–S batteries: functional separators promoting $Li^+$ transport and polysulfide trapping†

Sara Gullace, [a] Matteo Abruzzese,[b] Luca Cusin,[a] Gabriele Saleh,[c] Sanjay B. Thorat,[b] Agnese Gamberini,[b] Sebastiano Bellani,[b] Artur Ciesielski, [a] Francesco Bonaccorso[bc] and Paolo Samorì *[a]

Lithium–sulphur batteries (LSBs) prevail as a viable alternative to Li-ion batteries due to their high theoretical specific capacity (1672 mA h $g_S^{-1}$). However, the formation of soluble polysulfides and their shuttle from the cathode to the anode cause irreversible capacity loss and uncontrolled self-discharge, limiting the performance of commercially available prototypes. In this work, we present a comparative analysis of two Kagome-shaped imine-based covalent organic frameworks (COFs) as functional modifiers for polypropylene (Celgard) separators in LSBs. We demonstrate, by using the KS60@Celgard separator modified with an optimized content of COF with the thienothiophene linker, the realization of LSBs reaching a specific discharge capacity of 850 mA h $g_S^{-1}$ at C5. The proposed separator has an extraordinarily high $Li^+$ diffusion coefficient ($D_{Li^+}$) of 1.6 × $10^{-7}$ $cm^2$ $s^{-1}$ at the first cathodic peak, as well as the lowest $S_8$ : $Li_2S_x$ content ratio in the *ex situ post mortem* XPS analysis. These findings demonstrate that the use of separators modified with COFs allows the mitigation of shuttle effect, and is further accompanied by an efficient oxidation of $Li_2S_x$ to $S_8$ (electrocatalytic effect). The equivalent K60@Celgard, based on a COF carrying a phenyl linker, results in LSBs with a specific discharge capacity of 599 mA h $g_S^{-1}$. This work highlights the synergistic effect of polysulfide retention, selective $Li^+$ sieving and electrocatalytic activity of COF-modified Celgard separators in the development of high-performance LSBs.

Received 6th June 2024
Accepted 15th August 2024

DOI: 10.1039/d4ta03930k

rsc.li/materials-a



## Introduction

The fabrication of high-energy density rechargeable batteries marks a pivotal advancement in extending the specific capacity of well-established systems, namely lithium-ion batteries.[1] This progress is essential for facilitating the transition to electrified road transport and for applications within the aviation industry.[2,3] Among the various battery solutions, lithium–sulphur batteries (LSBs) are considered as extremely competitive configurations due to their high theoretical specific capacity of 1672 mA h $g_S^{-1}$, and the abundance and low cost of sulphur used as the cathode active material.[4,5] Unlike Li-ion batteries, LSBs rely on multi-electron conversion reactions. In a simplified and ideal discharge process, elemental octasulphur ($S_8$) is reduced by breaking its cyclic structure into chains of high-order lithium polysulfides, $Li_2S_x$ ($6 < x \leq 8$). Subsequently, additional redox reactions occur, leading to the formation of low-order polysulfides and ultimately yielding $Li_2S$.[6] Unfortunately, this conversion mechanism results in the formation of various soluble polysulfide intermediates in different oxidation states,[7,8] characterized by relatively high mobility in the battery electrolyte (~$10^{-10}$ $m^2$ $s^{-1}$).[2,9] This phenomenon is known as the "shuttle effect", wherein soluble $Li_2S_x$ species migrate from the cathode to the anode, causing uncontrolled self-discharge.[10] Consequently, this impedes the recharging process of polysulfide back to elemental sulphur and initiates the corrosion of Li metal anodes. These issues are responsible for the low coulombic efficiency and severe capacity fading.[11] Moreover, the multi-step redox process involves a liquid–solid phase transition to generate $Li_2S_2$ and $Li_2S$ species in the last reduction step.[8] The sluggish kinetics of this liquid–solid transition leads to incomplete $Li_2S$ deposition and consequently restricts the specific discharge capacity and rate performance.[5,12] Additionally, the low conductivity of sulphur-related species (5 × $10^{-30}$ S $cm^{-1}$ at 25 °C)[13] hampers the overall polysulfide utilization, resulting in a gradual depletion of active materials and, thus, insufficient cyclability.[14,15] Because of these reasons, efforts are made to optimize the design of LSBs. On one hand, these involve a scaffolding strategy that exploits the

[a]Institut de Science et d'Ingénierie Supramoléculaires, Université de Strasbourg, CNRS, 8 allée Gaspard Monge, 67000, Strasbourg, France. E-mail: samori@unistra.fr
[b]BeDimensional S.p.A., Via Lungotorrente Secca, 30R, 16163 Genova, Italy
[c]Istituto Italiano di Tecnologia, Via Morego, 30, 16163 Genova, Italy

† Electronic supplementary information (ESI) available. See DOI: https://doi.org/10.1039/d4ta03930k

incorporation of electrically conductive nano-porous carbons and polymers in the cathode with the aim of effectively encapsulating the sulphur, while mitigating the formation of a passivating $Li_2S_2/Li_2S$ layer on the sulphur. Additionally, these encapsulating materials serve as physical barriers against the polysulfide shuttle.[15–17] On the other hand, the separator also plays a significant role by facilitating the diffusion of $Li^+$, beyond preventing electrical contact between cathode and anode.[14,18] In this context, the presence of an additional layer atop the separator, regardless of its composition, might have a positive effect on the cell electrochemical performance. This is due to its ability to hinder the shuttle of high-order polysulfides by extending the diffusion pathway from the cathode to the anode side.[2] However, it is crucial that the materials used as modifiers for the separator are chosen meticulously to impart specific functionalities, such as retaining polysulfides, enhancing electrical conductivity, or improving the kinetics of conversion reactions.[2,19]

A plethora of materials have been employed as functional separator modifiers, spanning from zero-dimensional (0D)[20] to two-dimensional (2D) carbon-based materials,[21] polymers,[22] inorganic[23] or hybrid polymer/inorganic materials.[24–26] It has been demonstrated that the functional separator should provide a perfect balance between physical properties (*i.e.*, surface area, pore volume and capillary forces) and electrochemical properties ($Li^+$ transfer, C-rate capability and cycling stability). Such balance can be achieved using materials with ordered hierarchical pores.[2,27]

Based on this rationale, metal–organic frameworks (MOFs) and covalent organic frameworks (COFs) represent a viable attractive alternative as separator modifiers. In particular, COFs possess a highly ordered lattice structure and discrete hierarchical pores capable of interacting with ions and molecules.[28,29] Furthermore, *ad hoc* chemical design enables the synthesis of COFs combining high surface area, low density, high stability to acids and bases, easy functionalization and ample combinations of building blocks, making them highly suitable for a wide range of applications, spanning from adsorption of contaminants and molecular sieving to catalysis, sensing, proton conduction and energy storage.[30–33] In recent years, 2D COFs have been applied as sulphur-hosting materials in LSB cathodes, taking advantage of the highly ordered porous structure resulting from the stacking of the 2D planar sheets in one direction: this characteristic can provide accessible voids for sulphur impregnation, while suppressing the diffusion-driven loss of soluble polysulfides.[34–36] However, the low electrical conductivity of this organic material composites represents an important weakness for the realization of practical electrodes.[37,38] Nevertheless, COF-based materials offer structural designability to obtain abundant active sites for polysulfide adsorption, and accessible channels to facilitate the transport of $Li^+$ and indirectly inhibit the growth of Li dendrites, enabling their use in advanced separators beyond their applications as electrode materials.[39–42] Cao *et al.* reported the use of a sulfonate-rich COF-modified separator based on lithiated 3,5-triformylphloroglucinol and 2,5-diaminobenzenesulfonic acid (TpPa-$SO_3$Li), obtaining a LSB with a specific discharge capacity of 939.4 mA h $g_S^{-1}$ at C5, along with 55.1% capacity retention after 100 galvanostatic charge/discharge (GCD) cycles, when using a cathode with a sulphur loading of 1.5 $mg_S$ $cm^{-2}$.[43] Similarly, Xu *et al.* used TpPa-$(SO_3)_2$ as a separator modifier, obtaining a specific discharge capacity of 879 mA h $g_S^{-1}$ at C10, in a LSB with a sulphur loading of 1.3–1.5 $mg_S$ $cm^{-2}$ in the cathode. Additionally, they achieved a specific discharge capacity of 1036 mA h $g_S^{-1}$ at C5 with 82.5% capacity retention over 100 CGD cycles, when using a cathode with a sulphur loading of 3.2 $mg_S$ $cm^{-2}$ and carbon nanotubes as advanced conductive additives[44] (instead of the carbon black used in the low sulphur loading LSB and in ref. 43). Notably, these results were achieved using flat (carbon-coated) Al foils as current collectors, avoiding gas diffusion layers commonly reported for high sulphur-mass normalized performances, but leading to non-practical cell configurations (in terms of either gravimetric or volumetric full cell metrics).[45,46]

While hexagonal COF topology has received the greatest attention among LSB separators,[43,44] in this work we present a comparative analysis of two Kagome-shaped imine-based COFs as functional modifiers for prototypical Celgard separators in LSBs. We discovered that COF KS1, carrying a thienothiophene linker, allows the corresponding LSB, encountering Celgard separators modified with a 60 wt% COF KS1-based coating, to achieve a specific discharge capacity of 850 mA h $g_S^{-1}$ at C5. Importantly, this cell was built with a cathode with a sulphur loading of 2.4 $mg_S$ $cm^{-2}$ and a flat carbon-coated Al current collector. The proposed LSB exhibited a capacity retention of 74.1% after 190 GCD cycles. This result is accompanied by an extraordinary $Li^+$ diffusion coefficient ($D_{Li^+}$) as high as $1.6 \times 10^{-7}$ $cm^2$ $s^{-1}$ at the first cathodic peak. Under the same operating conditions, the use of a separator coating based on 60 wt% of COF K1, carrying a phenyl linker, results in LSBs with a specific discharge capacity of 599 mA h $g_S^{-1}$. Under the same operating conditions, also the increase of COF KS1 content in the separator coating (*i.e.*, 80 wt%) results in a LSB with a poor specific discharge capacity of 577 mA h $g_S^{-1}$. The influence of the nature of the linker and the COF content on the performance of COF-modified Celgard separators for LSBs is also confirmed by *post mortem ex situ* X-ray photoelectron spectroscopy (XPS) and scanning electron microscopy (SEM) analysis. Our approach provides a strategy to cooperatively exploit the polysulfide retention, the selective $Li^+$ sieving and the electrocatalytic activity of layered porous materials for the fabrication of high-energy density LSBs.

## Experimental section

### Materials

*N*,*N*,*N*,*N*-Tetrakis(4-aminophenyl)-1,4-phenylenediamine (98%) (TPDA) was purchased from abcr GmbH Germany; terephthalaldehyde (TPA) (99%), sulphur (99.998% trace metals basis), LiTFSI (99.95% trace metals basis), and lithium nitrate ($LiNO_3$, 99.99% trace metals basis) were purchased from Merck. Thieno[3,2-*b*]thiophene-2,5-dicarboxaldehyde (TTDA) was purchased from TCI. Carbon black (Super P) and polymer binder (Solef® 6020 PVDF) were purchased from Alfa Aesar and Solvay,

 

respectively. The polypropylene separator (Celgard® 2400) was supplied by Celgard. The carbon-coated Al cathode current collector and Li chips were purchased from MTI Corporation. The CR2032 coin cell cases and other coin cell components, made of stainless steel SS304, were purchased from MTI Corporation. Mesitylene (98%), benzyl alcohol (99%), acetic acid (glacial) and DMF were purchased from Fisher Scientific, *n*-pentane was purchased form Carlo Erba Reagents, while 1,3-dioxolane (DOL), 1,2-dimethoxyethane (DME), and *N*-methyl-2-pyrrolidone (NMP) were acquired from Sigma-Aldrich. Prior to use, DOL and DME solvents were dried with 3 Å rods, size 1/16 in. Sigma-Aldrich molecular sieves. All other solvents were used as received. Milli-Q grade water was used in all described experiments.

### Synthesis of COF K1 (TPDA–PTA)

In a 35 mL pressure resistant Schlenk tube, 236 mg of TPDA (0.5 mmol, 1 equiv.) and 134 mg of PTA (1 mmol, 2 equiv.) were dispersed by ultrasonication (30 min) in a mixture of benzyl alcohol (4 mL), mesitylene (4 mL), and water (0.2 mL). Then, glacial acetic acid (1 mL) was added, and the suspension was degassed by three freeze–pump–thaw cycles. The polycondensation reaction was carried out at 120 °C for 72 h in an oven. After cooling down, the solid precipitate was filtered off and washed thoroughly with DMF. The wet powders were then subjected to Soxhlet extraction with acetone for 12 h. Next, the acetone was exchanged with *n*-pentane (Soxhlet extraction, 2 h) and finally the powder was dried under vacuum at 80 °C overnight. The product was obtained as an insoluble red solid with a yield of 72%.

### Synthesis of COF KS1 (TPDA–TTDA)

In a 35 mL pressure resistant Schlenk tube, 236 mg of TPDA (0.5 mmol, 1 equiv.) and 196 mg of TTDA (1.0 mmol, 2 equiv.) were dispersed by ultrasonication (30 min) in a mixture of benzyl alcohol (5 mL), mesitylene (5 mL), and water (0.5 mL). Then glacial acetic acid (3 mL) was added, and the suspension was degassed by three freeze–pump–thaw cycles. The polycondensation reaction was carried out at 120 °C for 72 h in an oven. After cooling down, the solid precipitate was filtered off and washed thoroughly with DMF. The wet powders were then subjected to Soxhlet extraction with acetone for 12 h. Next, the acetone was exchanged with *n*-pentane (Soxhlet extraction, 2 h) and finally the powder was dried under vacuum at 80 °C overnight. The product was obtained as an insoluble red solid with a yield of 60%.

### COF-modified separator fabrication

The COF-based slurries were prepared by mixing COF K1 or KS1 together with SP and PVDF in NMP in different weight ratios. The COF-based slurries were then coated on Celgard2400 separators using the doctor blade technique, setting a blade height of 200 μm. Subsequently, the coated separators were dried at room temperature overnight and, finally, they were cut into 18 mm-diameter disks and dried overnight under vacuum at 35 °C to remove solvent residues and absorbed moisture. Table S1† reports the acronyms and characteristics of each COF-modified separator, compared with the bare Celgard2400 separator, including their areal weight.

### Cathode preparation

In a round bottom flask, the sulphur–Super P (S–SP) composite was prepared by mixing elemental sulphur and Super P with a weight ratio of 70 : 30 under magnetic stirring at 125 °C for ~1 h, until complete sulphur melting and homogenization. The resulting composite was subsequently cooled down to room temperature and ground in a mortar. The S–SP composite was mixed through an appropriate mixer with SP and PVDF binder homogeneously dispersed in NMP, to obtain a slurry with 80 : 10 : 10 w/w ratio. The LSB cathodes were then obtained through casting of the prepared slurry on carbon-coated Al foil by means of a doctor blade with a height of 250 μm. The sample was subsequently dried at 50 °C for 3 h. Finally, the electrodes were cut into 14 mm-diameter disks (geometrical area of 1.54 $cm^2$) and dried overnight under vacuum at 35 °C to remove traces of water and solvents.

### Cell assembly

The effect of the COF-modified separators on the electrochemical performance of LSBs was evaluated in CR2032 coin cell formats. The cells were assembled by stacking lithium chips (diameter of 14 mm) as the anode with COF-modified separators and the above-described cathode as the working electrode, in a MBraun argon-filled glovebox with $H_2O$ and $O_2$ contents below 1 ppm. The electrolyte consisted of 1 mol of LiTFSI and 1 mol of $LiNO_3$ dissolved in 1 kg of DOL : DME 1 : 1 w/w mixture. An electrolyte to sulphur (E/S) ratio of 15 μL $mg_S^{-1}$ was used to fill the coin cells.

### Characterization

Scanning electron microscopy (SEM) images were acquired using a JEOL JSM-6490LA SEM analytical (low-vacuum) instrument with a thermionic electron gun equipped with a tungsten source or a FEI Quanta 250 FEG Scanning Electron Microscope, operating in a high vacuum mode, after coating the substrate with 10 nm-thick gold using a sputter coater (ambient temperature, pressure in $10^{-4}$ mbar range in a $N_2$ atmosphere, sputtered for 20 s from a solid gold target at a current of 60 mA). Powder X-ray diffraction (PXRD) spectra were recorded using a D8 Advanced Bruker diffractometer ($2\theta$ resolution: ±0.01°) in the Bragg–Brentano geometry. The diffractometer used Cu Kα radiation (wavelength $\lambda = 0.154\,056$ nm) at 40 kV and 40 mA and a LynxEye_2 detector (1D mode). Two Soller slits (Cu, 2.5 mm) have been applied to the primary and secondary optics. In the latter, a Ni stopper has been added to filter Cu kα radiation. XRD data were collected from 2 to 30° ($2\theta$) with a step of 0.02° and an acquisition time of 1 s per step. Fourier transform-infrared (FTIR) spectra were acquired with a Thermo Scientific Nicolet iS50 FT-IR spectrometer equipped with the ATR diamond and a DTGS KBr detector. Thermogravimetric analysis (TGA) decomposition curves were recorded using a Mettler Toledo TGA/SDTA851e system in the range of 25–800 °C under a nitrogen atmosphere and with a heating rate of 10 °C $min^{-1}$.

X-ray photoelectron spectroscopy (XPS) characterization was performed using a Thermo Scientific K-alpha X-ray photoelectron spectrometer, equipped with an aluminum X-ray source (energy 1.4866 keV) at a vacuum level of $10^{-8}/10^{-9}$ mbar in the analysis chamber. The spot size of the X-ray beam was fixed at 200 μm. Cyclic voltammetry (CV) measurements were performed with 0.1 mV $s^{-1}$ scan rate in a potential window of 1.8–2.8 V *vs.* $Li^+/Li$ on a Biologic BCS-805 battery tester, while electrochemical impedance spectroscopy (EIS) measurements were performed in a frequency range of 500 kHz to 0.1 Hz with an amplitude of 10 mV using a VMP3B Multichannel Potentiostat. Galvanostatic charge–discharge measurements were performed at C5 (1C = 1672 mA $g_S^{-1}$) in a 1.9–2.8 V *vs.* $Li^+/Li$ potential window using a MACCOR series 4000 battery cycler. The C-rate convention (*n*C) is used in this manuscript, with 1C being defined as full theoretical lithium discharge/charge in one hour and *n* as the time (h) for complete charge or discharge at the nominal (theoretical) capacity.

## Results and discussion

### COF synthesis and characterization

A schematic representation of COF K1 synthesis from TPDA and TPA, and COF KS1 from TPDA with TTDA is shown in Scheme 1a. The solvothermal synthesis of the two Kagome-structured imine-based COFs K1 and KS1 yields a powder composed of nanoflower-like crystallites and nanospheres, respectively, as shown in the ESI (Fig. S1a and b†).

The FTIR analyses of K1 and KS1 exhibit the typical spectral features of an imine-linked COF (Fig. S1c†), with bands ascribed to the imine C=N stretching vibration at 1616 $cm^{-1}$ for K1 and at 1606 $cm^{-1}$ for KS1.[47] Moreover, the C=O stretching vibration bands (1683 $cm^{-1}$ for TPA and 1653 $cm^{-1}$ for TTDA) and the N–H vibration bands (3470–3320 $cm^{-1}$ and 1620 $cm^{-1}$) appear with significantly reduced intensities in the COFs, compared to the starting monomers. The most prominent bands at 1494 $cm^{-1}$ for K1 and 1479–1497 $cm^{-1}$ for KS1 are ascribed to the aromatic ring stretching modes.[48]

The PXRD analysis of TPDA–TPA and TPDA–TTDA provided evidence for a good degree of crystallinity of the two materials (Fig. S1d†). For COF K1, the main reflections at 2.5°, 4.2°, 4.9°, 6.4°, 8.7°, and 21.8° are ascribed to the (100), (110), (200), (210), (310), and (001) planes, respectively. In the case of COF KS1, the same pattern, slightly downshifted, was found at 2.3°, 3.9°, 4.6°, 6.0°, 8.2° and 21.1°, respectively. These PXRD patterns are in line with previous studies, which assigned to both COFs a Kagome structure with eclipsed stacking of the polymeric layers.[47,49,50] However, our preliminary density functional theory simulations show unequivocally that the eclipsed structure is energetically unfavourable compared to other types of stacking (ESI Note 1†). The complexity of the reaction mechanism for the synthesis of COFs with the interplay between thermodynamic and kinetic effects,[51] and, consequentially, their structural complexity would require a more accurate interpretation of the experimental PXRD patterns and those of the simulated structures to determine reliably the stacking geometry of these COFs (see also Fig. S13† and related discussion). However, this study goes beyond the scope of the present work.

TGA was performed to shed light onto the thermal stability of KS1 COF in a $N_2$ atmosphere, while the analogous characterization of COF K1 has been already reported in our previous work.[32] Fig. S1e† shows that KS1 is extremely robust and stable, with an initial 3 wt% loss in the temperature range between 110 °C and 170 °C, associated with the loss of physisorbed species, followed by its decomposition occurring after 430 °C.

COFs K1 and KS1 were characterized by XPS (Fig. S2 in the ESI†). The COF K1 high-resolution spectrum for C 1s core levels presents five deconvoluted sub-peaks at 284.4, 285.5, 286.3, 287.4 and 290.9 eV, which can be ascribed to the typical C=C, C–C, C–N, C=N chemical environments in the imine COFs, and the π–π* satellite for aromatic carbons, respectively. The N 1s spectrum confirms the presence of the triphenylamine moiety and the imine linkage, in addition to a small band for protonated amine, peaking at 398.4, 399.4 and 401.2 eV, respectively (Fig. S2a and b†). Similarly, the XPS spectra for COF KS1 can be deconvoluted to the same components, with the addition of a contribution from C–S at 287 eV in the C 1s core level (Fig. S2d†), as well as the S 2s and S 2p peaks (228.8 and 164.8 eV) in the survey spectrum (Fig. S2g†). In particular, the S 2p high-resolution spectra show the typical $2p_{3/2}$ and $2p_{1/2}$ doublets with an energy gap of 1.18 eV (Fig. S2f†).

### COF-modified separator fabrication and characterization

COF-modified separators were fabricated by applying COF-based slurries, in the form of a thin layer, with varying weight ratios of COF : Super P carbon black (SP) : polyvinylidene fluoride (PVDF), onto a prototypical battery separator, *i.e.*, Celgard 2400 (Scheme 1b). In particular, separators coated with thin films with 60 wt% K1 and KS1 were named K60@Celgard and KS60@Celgard, while the separator coated with a layer based on a higher content of KS1, *i.e.* 80 wt%, is hereafter referred to as KS80@Celgard. Fig. 1a–c and S3† show the XPS spectra of the investigated COF-modified separators, *i.e.*, K60@Celgard, KS60@Celgard and KS80@Celgard. The analysis reveals that the COFs K1 and KS1 maintain their structure in the composite coatings, while the appearance of a peak for F 1s in the survey spectrum is ascribed to the PVDF binder. SEM characterization shows that the COF K1 and KS1 morphologies are maintained, while sub-micrometric SP particles electrically connect COFs to each other (Fig. 1d–f). Fig. S4 in the ESI† shows the low-magnification SEM images of the pristine Celgard and COF-modified Celgard separators, as well as the SEM cross-sectional view of the pristine Celgard and the KS60@Celgard separator, evidencing the uniformity of the modified layers and thickness of the separator modifier, respectively (~20 μm).

### Electrochemical characterization of LSBs

The pristine and COF-modified separators were used to fabricate LSBs, whose structure is portrayed in Scheme 1c. Coin cells were assembled by stacking a sulphur cathode (sulphur loading of 2–3 $mg_S$ $cm^{-2}$), the pristine or COF-modified Celgard separator soaked in the electrolyte, and a Li anode. CV and EIS

 

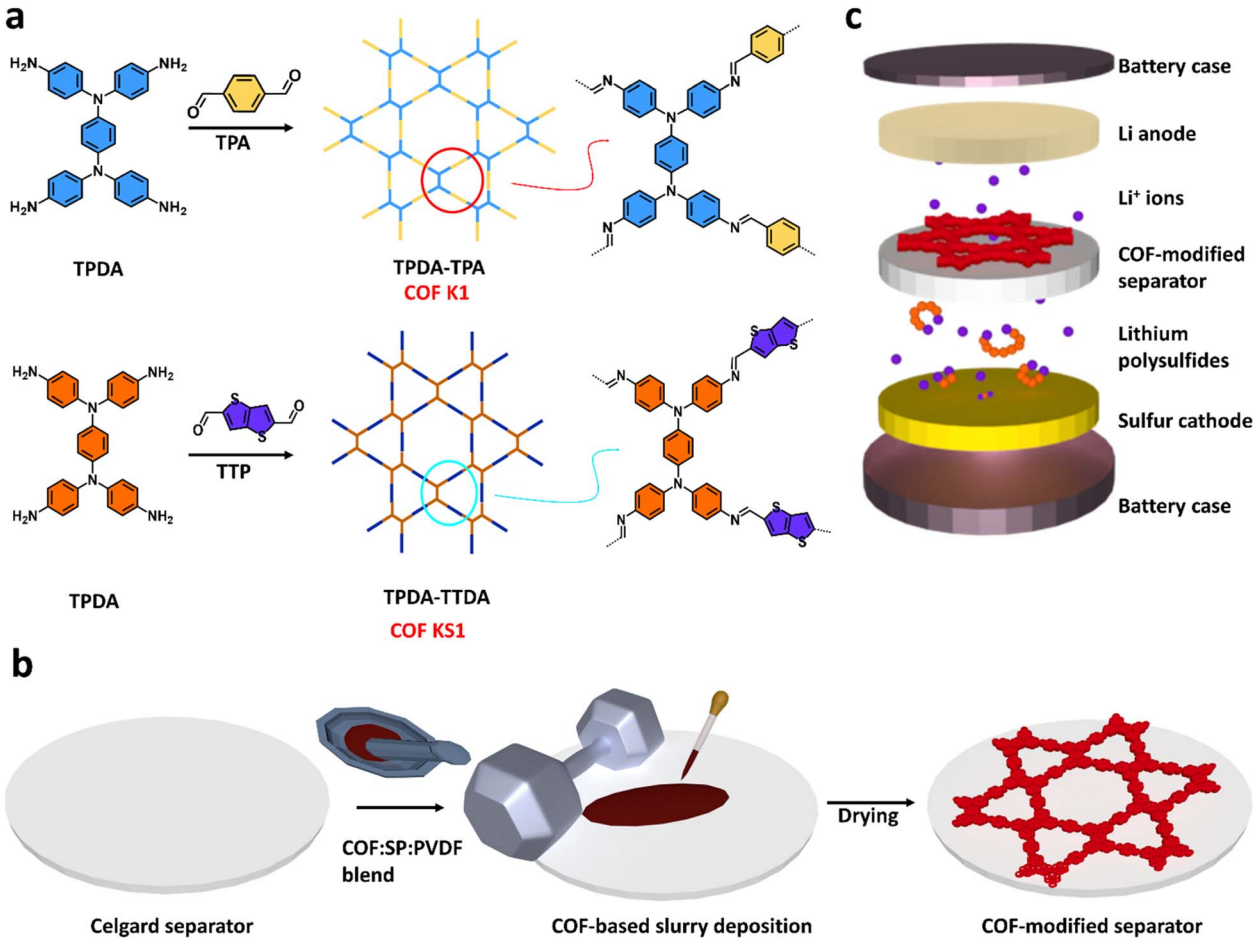


Scheme 1 (a) Schematic representation of the solvothermal synthesis of the two Kagome shaped imine-based COFs K1 and KS1. (b) Coating of a prototypical Celgard separator with the COF : SP : PVDF blend to prepare the COF-modified separator. (c) Sketch of a LSB in coin cell format, containing a sulphur cathode, the COF-modified separator and the Li anode. The ability of the separators to block the shuttle of $Li_2S_x$ is pictorially presented.

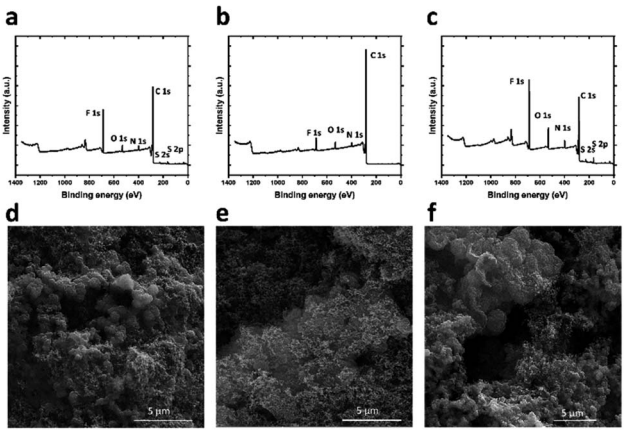


Fig. 1 (a)–(c) Survey XPS spectra for (a) KS60@Celgard, (b) K60@Celgard and (c) KS80@Celgard separators. (d)–(f) SEM images of the (d) KS60@Celgard, (e) K60@Celgard and (f) KS80@Celgard separators.

measurements were performed on the proposed LSBs to evaluate the electrochemical conversion processes and the evolution of the electrode/electrolyte interfaces, respectively, upon consecutive CV cycles. Fig. 2a–d show the CV curves measured for the LSBs assembled with pristine Celgard, KS60@Celgard K60@Celgard and KS80@Celgard separators, respectively. The cyclic voltammograms, recorded between 1.7 and 2.8 V *vs.* $Li^+/Li$ with different voltage scan rates ranging between from 0.05 to 0.25 mV $s^{-1}$, reveal the typical features associated with the conversion reactions involving Li, $S_8$ and polysulfides. At the lowest scan rate, two reduction peaks at 2.20 and 1.80 V *vs.* $Li^+/Li$, as well as a convoluted double oxidation peak extending from ~2.33 to ~2.42 V *vs.* $Li^+/Li$ are identified for the cell based on pristine Celgard. The negative peaks correspond to the reduction of $S_8$ to high-order ($Li_2S_x$, $4 \leq x \leq 8$) and low-order insoluble ($Li_2S_2$ and $Li_2S$) polysulfides, respectively. In the anodic region, the two peaks can be ascribed to the inverse conversion reactions of $Li_2S_2$ and $Li_2S$, yielding long-chain polysulfides and $S_8$.[52] For the cell based on KS60@Celgard, the same reduction peaks appear at 2.24 and 1.97 V *vs.* $Li^+/Li$, while the oxidation ones appear at 2.36 and 2.44 V *vs.* $Li^+/Li$. The CV analysis evidences that the batteries with KS60@Celgard and K60@Celgard exhibit the lowest overpotential (0.39 V) for the conversion reactions involving $Li_2S_2$ and $Li_2S$, indicating faster reaction kinetics compared to those observed for the

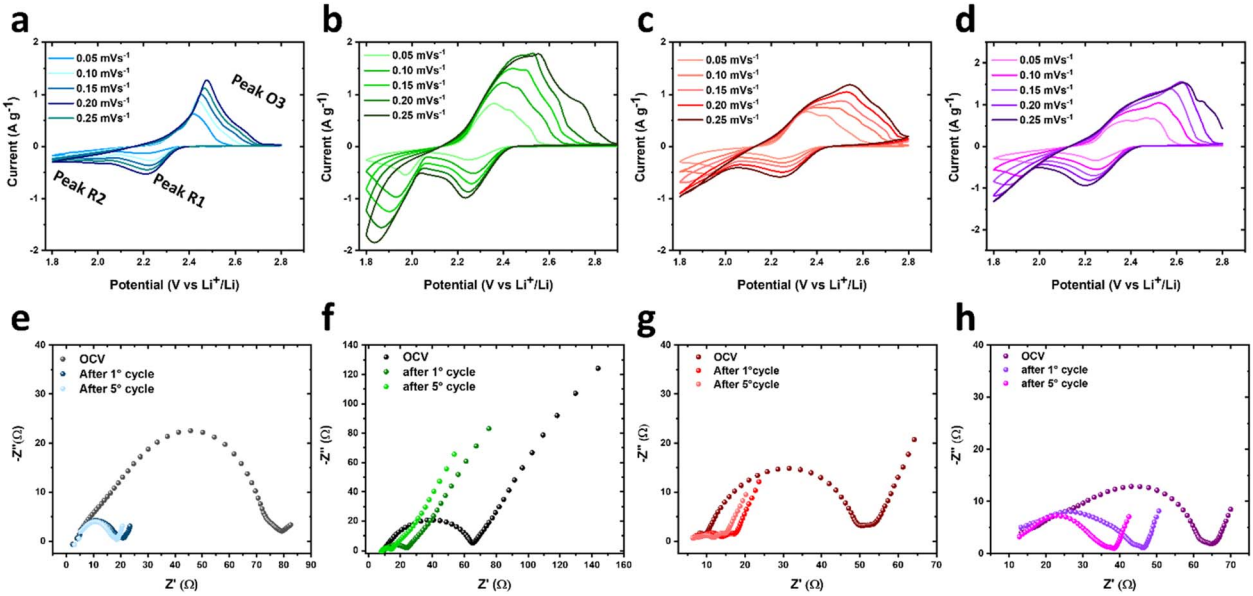


Fig. 2 (a)–(d) CV curves measured at different voltage scan rates ranging from 0.05 to 0.25 mV $s^{-1}$ for the LSBs based on (a) pristine Celgard, (b) KS60@Celgard, (c) K60@Celgard and (d) KS80@Celgard separators. (e)–(h) Nyquist plots measured for the LSBs based on (e) pristine Celgard, (f) KS60@Celgard, (g) K60@Celgard and (h) KS80@Celgard separators.

other cells.[53,54] The overpotentials for cells based on pristine Celgard and KS80@Celgard are 0.53 and 0.42 V, respectively.

Additionally, the $Li^+$ diffusion coefficient ($D_{Li^+}$, expressed in $cm^2\ mol^{-1}$) can be evaluated from the relationship between the peak current intensity $I_p$ and the square root of the potential scan rate $\nu$, as described by the Randles–Sevcik equation:

$$I_p = 0.4463zFAC_{Li}\sqrt{\frac{zF\nu D_{Li^+}}{RT}}$$

in which $z$ is the number of exchanged electrons in the electrochemical reaction, $F$ is the Faraday constant (96 485 C $mol^{-1}$), $A$ is the electrode geometric area (1.54 $cm^2$), $C$ stands for the estimated $Li^+$ concentration in the electrode volume expressed in mol $cm^{-3}$, $\nu$ is the scan rate in V $s^{-1}$, $R$ is the gas constant (8.314 J $mol^{-1}$ $K^{-1}$), and $T$ is the temperature in K. Thus, $I_p$ of the two reduction peaks R1 and R2 at ~2.2 and ~1.9 V *vs.* $Li^+$/Li, respectively, and the oxidation peak O3 at 2.4 V *vs.* $Li^+$/Li, were analysed as a function of $\nu^{1/2}$.[46] The linear fit of the obtained plots allows the determination of the slope for the calculation of $D_{Li^+}$ (Fig. S5, ESI†). The obtained values are summarized in Fig. S6 and Table S2 (ESI†). In all the analysed cells, $D_{Li^+}$ exhibits the highest value in correspondence of the reduction peak R1 at 2.2 V *vs.* $Li^+$/Li and decreases at the second discharge step associated with peak R2 at 1.95 V *vs.* $Li^+$/Li (Fig. S6 in the ESI†). This behaviour can be ascribed to the presence of a high concentration of soluble species with high ionic mobility, such as long-chain polysulfides, at R1. On the contrary, at R2, the most abundant species are short-chain polysulfides, which exhibit low solubility and low ionic mobility. The obtained data reveal that, compared to the pristine Celgard, all the COF-modified separators increase $D_{Li^+}$ due to the confined transportation of $Li^+$ within the one-dimensional (1D) channels featured by COF structures.[55] However, among the investigated LSBs, the highest $D_{Li^+}$ values were obtained in the cell based on the KS60@Celgard separator ($1.6 \times 10^{-7}$ $cm^2$ $s^{-1}$ at 2.2 V *vs.* $Li^+$/Li). This result suggests that KS60@Celgard allows selective sieving of $Li^+$.[56]

Electrochemical impedance spectroscopy measurements were further conducted on new cells in the 500 kHz to 100 mHz frequency range at the open circuit voltage (OCV) state, before the first CV cycle and after each CV cycle recorded at a voltage scan rate of 0.1 mV $s^{-1}$ (Fig. 2e–h). The resulting Nyquist plots were used to gain information on the charge transfer processes at the electrode/electrolyte interface. As shown in Table S3 in the ESI,† all the Nyquist plots were fitted with an appropriate equivalent circuit based on the following circuit elements: $R_e$, representing the electrolyte resistance and general series resistances; $R_i$ and $C_i$ (or $Q_i$), representing the resistance and capacitance (or constant phase element, CPE) related to the charge transfer processes at the electrode/electrolyte interface; an additional $R_wQ_w$ element at low frequency associated with the semi-finite diffusion of $Li^+$, and a final $Q_{diff}$ element, representing a CPE associated with the diffusion processes of redox species.[46,57] The EIS response substantially varies moving from the initial OCV state to the end of CV cycling. For all the studied LSBs, the total $R_{tot}$, given by the sum of the various resistances, decreases drastically. Interestingly, $R_{tot}$ reaches values as low as 6.1 ± 0.1 and 6.2 ± 0.2 Ω in the case of the cells based on KS60@Celgard and K60@Celgard separators, respectively, after 5 CV cycles. Furthermore, the phase angle Bode plot, shown in Fig. S7 (ESI†), provides insight into the $Li^+$ diffusion processes occurring in the cells. In particular, more negative values of phase angle in the low frequency region indicate rapid $Li^+$ diffusion.[58] The battery based on the KS60@Celgard separator

 

reaches the most negative phase angle of −51° at 0.1 Hz, while the use of Celgard, K60@Celgard and KS80@Celgard separators results in higher values, *i.e.* of −21°, −22° and −43°, respectively. Considering that the investigated cells differ only in the composition of the separator coating, these data indicate that the KS60@Celgard separator can efficiently ensure optimal $Li^+$ diffusion, outperforming the other separators.[56,58] The combination of EIS and CV data supports that the KS60@Celgard separator is the most efficient one in enabling selective $Li^+$ sieving.

The effect of the different separators on the LSB performances was then studied through GCD measurements. Fig. 3a shows the GCD profiles recorded at C10 rate (1C = 1672 mA $g_S^{-1}$) for LSBs based on the investigated separators (average sulphur loading ~2 mg $cm^{-2}$ and E/S ratio = 15 μL $mg_S^{-1}$). The GCD profiles are reported after 3 GCD cycles to ensure that the cells were sufficiently activated by appropriate electrode formation processes, allowing a reliable comparison of their performances. For all the investigated cells, it is possible to distinguish the two voltage plateaus, at ~2.3 and ~2.1 V, typically displayed by LSBs during their discharge. This discharging behaviour is well reversed during the charging step. The plateau at the highest voltage is generally associated with the formation of long-chain polysulfides ($Li_2S_x$, $4 \leq x \leq 8$), which are then reduced to low-order insoluble $Li_2S_2$ and $Li_2S$ during the second voltage plateau.[59,60] The cells based on Celgard, KS60@Celgard, K60@Celgard and KS80@Celgard separators show an initial specific discharge capacity of 879, 1050, 1072 and 906 mA h $g_S^{-1}$, respectively. Interestingly, all the COF-modified separator coatings induced an increase of the specific discharge capacity compared to the cell based on pristine Celgard. Thus, at low C-rate, the specific discharge capacity is highly influenced by the ability of the separator to trap high-order polysulfides: the presence of the COF porous structures ensures efficient polysulfide trapping, leading to high coulombic efficiency for the LSB conversion processes, without compromising $Li^+$ transport (see EIS and CV analyses).[61–63] This evidence can be explained by the presence of additional pore channels in the COF structures. New diffusion pathways in the modified separators can effectively hinder and retard the polysulfide migration and shuttle, with a positive effect on the $Li^+$ transport in the rest of the separator, and thus, on the overall electrochemical performance of the cell.[2] Scan rate-dependent CV analysis demonstrated that the COF-modified separators, in particular KS60@Celgard, can promote the diffusion of $Li^+$ (see Fig. 2a–d). In particular, polysulfide diffusion is affected by the chemical environment in the COF nanochannels.[32] Compared to polysulfides, $Li^+$ is less sterically hindered and positively charged. Thus, it can rapidly diffuse in the COF pores.[43,64] Furthermore, the cell overpotentials at the second discharge plateau are 130, 140, 220 and 170 mV for the cells containing pristine Celgard, KS60@Celgard, K60@Celgard and KS80@Celgard separators, respectively. Low values of overpotential can be associated with the efficient conversion of the long-chain polysulfides.[53] The data clearly indicate that COF KS1 facilitates polysulfide conversion processes, essentially acting as a catalyst for these reactions. Conversely, COF K1 seems to primarily function as a polysulfide retainer. Notably, a high content of COF KS1 on the separator causes an increase of the cell overpotential and a decrease of the cell capacity. Based on the previous CV and EIS analyses, an excessive content of COF KS1 can decrease $D_{Li^+}$ and, thus, the total charge transfer resistance and the specific discharge capacity of the corresponding cell.

Fig. 3b–e display the rate capability of the investigated LSBs, screening C-rates from C10 to 1C. Table S4 in the ESI† lists the specific discharge capacity measured at each C-rate. At low C-rate, the cells with the COF-modified separators displayed higher specific discharge capacities (*i.e.*, 933, 1028, 733 mA h

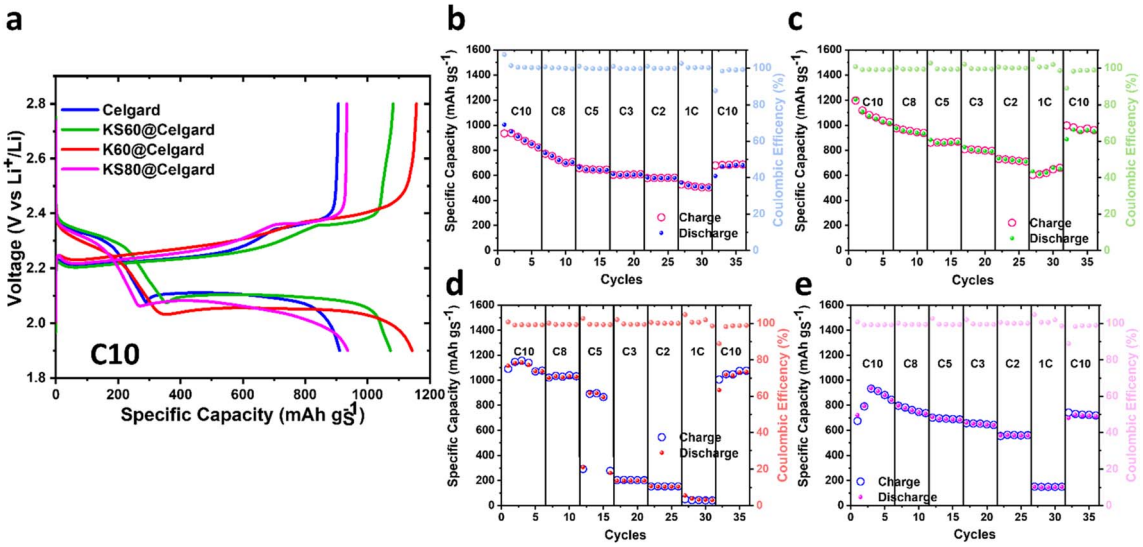


Fig. 3 (a) GCD profiles recorded at C10 of the LSBs (sulphur loading: ~2 $mg_S$ $cm^{-2}$; E/S ratio: 15 μL $mg_S^{-1}$, electrode geometric area: 1.54 $cm^2$) containing pristine Celgard, KS60@Celgard, K60@Celgard and KS80@Celgard separators. Rate performance from C10 to 1C of the Li–S batteries containing (b) pristine Celgard, (c) KS60@Celgard, (d) K60@Celgard and (e) KS80@Celgard separators.

$g_S^{-1}$ for KS60@Celgard, K60@Celgard and KS80@Celgard separators at C8) compared to the cell based on pristine Celgard (704 mA h $g_S^{-1}$ at C8), thanks to their ability to efficiently trap the long-chain polysulfides, thus, ensuring high S utilization. By increasing the C-rate, significant differences can be detected between the performances of cells based on different COF-modified separators. In particular, at 1C, the use of K60@Celgard and KS80@Celgard separators substantially reduces the specific discharge capacities to 44 and 150 mA h $g_S^{-1}$, respectively. In fact, at high C-rate, the capacity is strongly affected by the $Li^+$ transport.[61,62] Although K60@Celgard and KS80@Celgard separators can efficiently alleviate the polysulfide shuttle, they also slow down the transport of $Li^+$, as proved by the phase angle Bode plot and $D_{Li^+}$ analyses. The use of the KS60@Celgard separator ensures high specific discharge capacities at all the investigated C-rates, confirming a dual functional role of KS COF as a polysulfide retainer and a $Li^+$ sieve. Another important parameter for the LSBs is the discharge capacity loss, calculated from the discharge capacity ratio among the last discharge of the first and last GCD cycles acquired at C10. The discharge capacity loss is 17.5%, 6.4%, 0.3% and 15.5% for the cell based on pristine Celgard, KS60@Celgard, K60@Celgard and KS80@Celgard separators, respectively, indicating a satisfactory cyclability for the investigated LSBs, whose structural integrity is therefore preserved even after high-rate operation.[65]

Fig. 4 and S8 (ESI†) show the complete stability test and selected GCD profiles measured at C5 over 190 GCD cycles for the LSBs based on pristine Celgard, KS60@Celgard, K60@Celgard and KS80@Celgard separators, respectively. The measurements were performed after cell activation at low C-rates to ensure reproducible behaviours. For the cell based on pristine Celgard, the specific discharge capacity decreased significantly in the first GCD cycles, until stabilizing after *ca.* 20 GCD cycles. After the same number of GCD cycles, the specific discharge capacities of the cells based on KS60@Celgard and K60@Celgard separators reached their maximum values. This behaviour can be associated with the prolonged diffusion pathway from the cathode to the anode side when the functional COF coating is added to Celgard.[2] All the batteries displayed excellent cyclability for 190 GCD cycles with an average oulombic efficiency between 98 and 99%. The most performant cell based on KS60@Celgard (sulphur loading of 2.4 $mg_S\ cm^{-2}$) has shown the highest specific discharge capacity of 850 mA h $g_S^{-1}$ with 74.1% retention of its maximum specific discharge capacity after 190 GCD cycles.

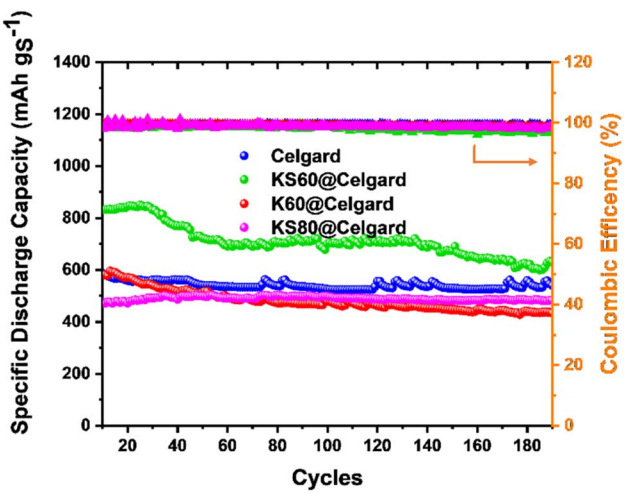


Fig. 4 Specific discharge capacity and coulombic efficiency over 190 GCD cycles at C5 measured for LSBs based on pristine Celgard, KS60@Celgard, K60@Celgard and KS80@Celgard separators.

Overall, the high specific discharge capacity at all the investigated C-rates, the capacity retention and coulombic efficiency of the cell based on the KS60@Celgard separator are explained by the ability of this separator to adsorb polysulfides and electrocatalytically promote the conversion of sulphur species, alleviating the shuttle effect and excessive conversion reaction overpotentials.[66] Based on literature data, Table S5† reports the comparison between the performances of different LSBs based on COF-based functional separators. Notably, this analysis evidences that most of the investigations on LSBs at the laboratory scale are performed using cathodes with low sulphur loading below 2 $mg_S\ cm^{-2}$, leading to low absolute energies that are not adequate for practical cells,[67,68] although resulting in higher specific discharge capacities compared to those reported in our work. Considering the high sulphur loading used in the present study, we believe that the performances of the fabricated LSBs, achieved with flat current collectors, are significant in the field.

### *Ex situ post mortem* analysis

After 190 GCD cycles at C5, the tested LSBs were disassembled in the charged state. *Post mortem* analysis was then performed through *ex situ* XPS characterization of the Celgard and COF-modified separators, assessing their surface compositions. Fig. 5 shows the S 2p core level spectra for all the investigated separators. Deconvolution was performed to distinguish the contribution from $Li_2S_x$ ($Li_2S$, terminal S–Li, bridged S–S) and elemental sulphur ($S_8$), as well as oxidized species such as $–SO_4$, and $–SO_2CF_3$, the latter deriving from the lithium LiTFSI electrolyte additive.[44,69–71] The binding energies and atomic percentage of the sulphur species corresponding to the deconvoluted bands are reported in Table S6 (ESI†). When COF-modified separators are used, the bands for $S_8$ and bridged S–S are red-shifted compared to those measured for pristine Celgard. This indicates an increased average oxidation state of sulphur, namely more abundance of long-chain $Li_2S_x$, because of the catalytic activity of the COFs towards the LSB conversion processes (Table S6†).[44,72] Interestingly, the ratio between the atomic content of S species corresponding to $S_8$ and $Li_2S_x$ bands varies as a function of the employed separator. In particular, it is *ca.* 1 : 5, 1 : 2, 1 : 4 and 1 : 4 for pristine Celgard, KS60@Celgard, K60@Celgard and KS80@Celgard separators, indicating that the redox reversibility of the different species depends on the characteristics of the separator.[73,74] The KS60@Celgard separator ensures the highest atomic ratio of S species corresponding to $S_8$ and $Li_2S_x$, demonstrating its electrocatalytic activity towards the LSB conversion processes, enabling an efficient oxidation of $Li_2S_x$ to $S_8$.[12]

 

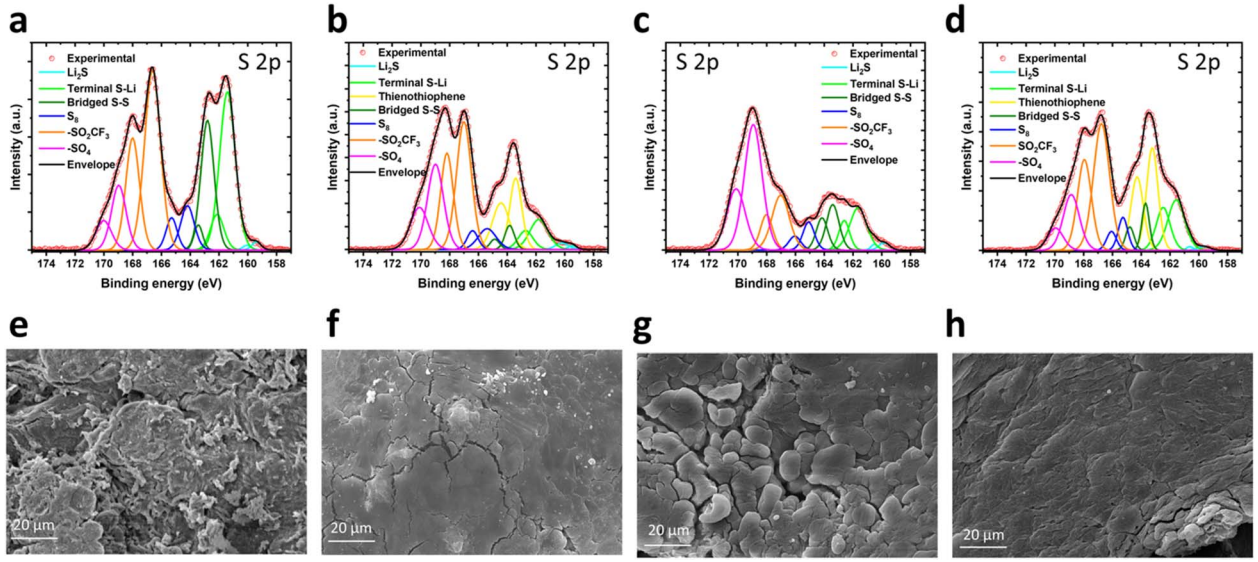


Fig. 5 *Ex situ* XPS spectra for S 2p core levels of (a) pristine Celgard, (b) KS60@Celgard, (c) K60@Celgard and (d) KS80@Celgard separators, obtained by disassembling the corresponding LSBs in the charged state after 190 GCD cycles. SEM images of Li anodes obtained by disassembling the LSBs, containing (e) pristine Celgard, (f) KS60@Celgard, (g) K60@Celgard, and (h) KS80@Celgard separators, in the charged state after 190 GCD cycles.

Additionally, morphological *post mortem* analysis was conducted on both Li anodes and separators by means of SEM measurements. It is well known that the shuttle of polysulfides corrodes the Li metal anode, leading to the depletion of active Li and exacerbating unevenness in the anode.[75] Once polysulfides diffuse to the anode side due to concentration gradients, they can rapidly react with the Li anode, forming insoluble species such as $Li_2S$ at the solid electrolyte interface (SEI).

This process contributes to increased SEI inhomogeneity, uneven Li plating/stripping and the formation of Li dendrites. Ultimately, the reaction between polysulfides and dendritic Li damages the original anode structure and yields inactive Li.[75–77] Fig. S9† shows the smooth surface of a standard fresh Li anode, while the comparison with those extracted from the cycled LSBs containing pristine Celgard, KS60@Celgard, K60@Celgard and KS80@Celgard separators is reported in Fig. 5e–h. In all cases, the anode surface morphology normally differs from the fresh Li because of repeated Li plating/stripping occurring during long-term GCD cycling. In particular, when the pristine Celgard separator is used, the Li anode evidences a highly inhomogeneous surface, with the deposition and growth of a large number of Li dendrites along with pits on the anode surface (Fig. 5e).[78,79] Differently, for the anodes of the LSBs based on KS60@Celgard, K60@Celgard and KS80@Celgard separators, the Li deposited after subsequent GCD cycles forms more uniform layers, especially when KS1 COF is used, without visible Li dendrite formation (Fig. 5f–h). Thus, the morphological *post mortem* analysis provides evidence that the modification of the separator by COF-based coatings reduces the polysulfide shuttle, which, in turn, mitigates the corrosion of the Li anode. Additionally, Fig. S10† shows that Li dendrites accumulated in the pristine Celgard separator, while no morphological modification occurred on KS60@Celgard, K60@Celgard and KS80@Celgard separators.

## Conclusion

In summary, we have fabricated COF-modified separators for LSBs using two Kagome shaped imine-based COFs, differing in the nature of the linker. We found that the two developed COFs significantly alleviate problems associated with the polysulfide shuttle and Li dendrite growth, extending the cycle life of the resulting LSBs. The use of the KS60@Celgard separator, based on coating with 60 wt% of COF with the thienothiophene linker, allows us to design and fabricate performant LSBs with a specific discharge capacity of 850 mA h $g_S^{-1}$ at C5 and a 74.1% capacity retention after 190 GCD cycles, using a cathode with a sulphur loading of 2.4 $mg_S$ $cm^{-2}$. In addition, the proposed LSBs have an extraordinarily high $D_{Li^+}$ of $1.6 \times 10^{-7}$ $cm^2$ $s^{-1}$, measured at the first cathodic peak, as well as the lowest $S_8$ : $Li_2S_x$ content ratio, as confirmed by the *ex situ post mortem* XPS analysis of the separators, obtained by disassembling charged LSBs after 190 GCD cycles. These results demonstrate that the shuttle effect mitigation is accompanied by an efficient oxidation of $Li_2S_x$ to $S_8$ (electrocatalytic effect), *i.e.*, high sulphur utilization. In parallel, the equivalent separator modified with a coating based on 60 wt% COF K1, carrying a phenyl linker, results in LSBs with a specific discharge capacity of 599 mA h $g_S^{-1}$, while the use of a higher content (80 wt%) of KS1 COF in the separator reduces the performances of the corresponding LSB (*e.g.*, specific discharge capacity of 577 mA h $g_S^{-1}$), under the same operating conditions (C5). Additionally, *post mortem* SEM analysis on the Li anodes recovered after cycling indicates that, differently from the case of pristine Celgard, the KS60@Celgard separator significantly mitigates polysulfide shuttle, as proved by the absence of Li dendrite growth. Overall, electrochemical investigations and *ex situ post mortem* XPS and SEM analyses elucidated the correlation between the nature of

the linker in the COF structure, the overall COF content in the separator and the performance of LSBs based on COF-modified Celgard separators. Overall, this work casts light onto the cooperativity among the polysulfide retention, the selective $Li^+$ sieving and the electrocatalytic properties of COF-modified Celgard separators for LSBs, paving the way towards the use of layered porous materials in high-performance LSBs.

## Data availability

Original data are available upon request to be sent to the corresponding author of the paper.

## Author contributions

S. G. conceived and coordinated the work, designed the experiments, interpreted the data, performed FT-IR, XPS and SEM characterization, and wrote the original manuscript with inputs from all the authors. M. A. and A. G. performed the LSB fabrication and electrochemical characterization. L. C. synthesized the COFs and performed their FT-IR, TGA, SEM and XRD characterization. G. S. performed the DFT simulations. S. B. T. performed SEM characterization. S. B. supervised the LSB fabrication and electrochemical characterization and performed manuscript review and editing. A. C., F. B. and P. S. performed manuscript review and editing, supervision and funding acquisition. The manuscript was written through contributions of all authors. All authors have given approval to the final version of the manuscript.

## Conflicts of interest

The authors declare no competing financial interest. M. A., S. B., S. B. T., A. G., and F. B. belong to BeDimensional S.p.A., a company commercializing two-dimensional materials.

## Acknowledgements

This project received funding from the European Union's Horizon 2020 Research and Innovation Program under the Marie Skłodowska-Curie project ULTIMATE Grant Agreement No. 813036, the European Union's Horizon 2020 Research and Innovation program under Grant Agreement No. 881603-GrapheneCore3, the European Union's GREENCAP Horizon Europe Research and Innovation Program under Grant Agreement No. 101091572, and the European Union's 2D-PRINTABLE Horizon Europe Research and Innovation Program under Grant Agreement No. 101135196. G. S. acknowledges funding from the programme MiSE-ENEA under the Grant "Italian Energy Materials Acceleration Platform – IEMAP" and the CINECA award under the ISCRA initiative, for the availability of high-performance computing resources and support. P. S. acknowledges financial support through the ANR through the Interdisciplinary Thematic Institute SysChem *via* the IdEx Unistra (ANR-10-IDEX-0002) within the program Investissement d'Avenir, the Foundation Jean-Marie Lehn and the Institut Universitaire de France (IUF).

## Notes and references

1 X. Judez, G. G. Eshetu, C. Li, L. M. Rodriguez-Martinez, H. Zhang and M. Armand, *Joule*, 2018, **2**, 2208–2224.
2 Y. C. Jeong, J. H. Kim, S. Nam, C. R. Park and S. J. Yang, *Adv. Funct. Mater.*, 2018, **28**, 1707411.
3 Strategic Energy Technology Plan, **https://energy.ec.europa.eu/topics/research-and-technology/strategic-energy-technology-plan_en**.
4 Y. Chen, T. Wang, H. Tian, D. Su, Q. Zhang and G. Wang, *Adv. Mater.*, 2021, **33**, 2003666.
5 Q. Shao, S. Zhu and J. Chen, *Nano Res.*, 2023, **16**, 8097–8138.
6 W. Brehm, V. Marangon, J. Panda, S. B. Thorat, A. E. del Rio Castillo, F. Bonaccorso, V. Pellegrini and J. Hassoun, *Energy Fuels*, 2022, **36**, 9321–9328.
7 D. Zheng, D. Liu, J. B. Harris, T. Ding, J. Si, S. Andrew, D. Qu, X.-Q. Yang and D. Qu, *ACS Appl. Mater. Interfaces*, 2017, **9**, 4326–4332.
8 D. Meggiolaro, M. Agostini and S. Brutti, *ACS Energy Lett.*, 2023, **8**, 1300–1312.
9 C. Park, A. Ronneburg, S. Risse, M. Ballauff, M. Kanduč and J. Dzubiella, *J. Phys. Chem. C*, 2019, **123**, 10167–10177.
10 Y. V. Mikhaylik and J. R. Akridge, *J. Electrochem. Soc.*, 2004, **151**, A1969.
11 Y. Liu, Y. Elias, J. Meng, D. Aurbach, R. Zou, D. Xia and Q. Pang, *Joule*, 2021, **5**, 2323–2364.
12 R. Fang, H. Xu, B. Xu, X. Li, Y. Li and J. B. Goodenough, *Adv. Funct. Mater.*, 2021, **31**, 2001812.
13 J. Wang, S. Y. Chew, Z. W. Zhao, S. Ashraf, D. Wexler, J. Chen, S. H. Ng, S. L. Chou and H. K. Liu, *Carbon*, 2008, **46**, 229–235.
14 H. Yao, K. Yan, W. Li, G. Zheng, D. Kong, Z. W. Seh, V. K. Narasimhan, Z. Liang and Y. Cui, *Energy Environ. Sci.*, 2014, **7**, 3381–3390.
15 L. Xiao, Y. Cao, J. Xiao, B. Schwenzer, M. H. Engelhard, L. V. Saraf, Z. Nie, G. J. Exarhos and J. Liu, *Adv. Mater.*, 2012, **24**, 1176–1181.
16 N. Jayaprakash, J. Shen, S. S. Moganty, A. Corona and L. A. Archer, *Angew. Chem., Int. Ed.*, 2011, **50**, 5904–5908.
17 X. Ji, K. T. Lee and L. F. Nazar, *Nat. Mater.*, 2009, **8**, 500–506.
18 C. Li, R. Liu, Y. Xiao, F. Cao and H. Zhang, *Energy Storage Mater.*, 2021, **40**, 439–460.
19 Z. Wei, Y. Ren, J. Sokolowski, X. Zhu and G. Wu, *InfoMat*, 2020, **2**, 483–508.
20 J. Breczko, M. Wysocka-Żołopa, E. Grądzka and K. Winkler, *ChemElectroChem*, 2024, e202300752.
21 A. Kim, S. H. Oh, A. Adhikari, B. R. Sathe, S. Kumar and R. Patel, *J. Mater. Chem. A*, 2023, **11**, 7833–7866.
22 X. Chen, C. Zhao, K. Yang, S. Sun, J. Bi, N. Zhu, Q. Cai, J. Wang and W. Yan, *Energy Environ. Mater.*, 2023, **6**, e12483.
23 Y. Wang, T. Guo, E. Alhajji, Z. Tian, Z. Shi, Y.-Z. Zhang and H. N. Alshareef, *Adv. Energy Mater.*, 2023, **13**, 2202860.
24 J. Pu, T. Wang, Y. Tan, S. Fan and P. Xue, *Small*, 2023, **19**, 2303266.
25 J.-Q. Huang, Q. Zhang and F. Wei, *Energy Storage Mater.*, 2015, **1**, 127–145.

26 T.-Z. Zhuang, J.-Q. Huang, H.-J. Peng, L.-Y. He, X.-B. Cheng, C.-M. Chen and Q. Zhang, *Small*, 2016, **12**, 381–389.
27 M. Wang, H. Zhang, W. Zhou, X. Yang, X. Li and H. Zhang, *J. Mater. Chem. A*, 2016, **4**, 1653–1662.
28 C. S. Diercks and O. M. Yaghi, *Science*, 2017, **355**, eaal1585.
29 K. Geng, T. He, R. Liu, S. Dalapati, K. T. Tan, Z. Li, S. Tao, Y. Gong, Q. Jiang and D. Jiang, *Chem. Rev.*, 2020, **120**, 8814–8933.
30 Y. Lu, Z.-B. Zhou, Q.-Y. Qi, J. Yao and X. Zhao, *ACS Appl. Mater. Interfaces*, 2022, **14**, 37019–37027.
31 G. Das, B. P. Biswal, S. Kandambeth, V. Venkatesh, G. Kaur, M. Addicoat, T. Heine, S. Verma and R. Banerjee, *Chem. Sci.*, 2015, **6**, 3931–3939.
32 S. Gullace, L. Cusin, F. Richard, N. Israfilov, A. Ciesielski and P. Samorì, *Adv. Mater. Interfaces*, 2023, **10**, 2300124.
33 H. Peng, S. Huang, V. Montes-García, D. Pakulski, H. Guo, F. Richard, X. Zhuang, P. Samorì and A. Ciesielski, *Angew. Chem., Int. Ed.*, 2023, **62**, e202216136.
34 H. Liao, H. Ding, B. Li, X. Ai and C. Wang, *J. Mater. Chem. A*, 2014, **2**, 8854–8858.
35 H. Liao, H. Wang, H. Ding, X. Meng, H. Xu, B. Wang, X. Ai and C. Wang, *J. Mater. Chem. A*, 2016, **4**, 7416–7421.
36 Y. Meng, G. Lin, H. Ding, H. Liao and C. Wang, *J. Mater. Chem. A*, 2018, **6**, 17186–17191.
37 Z. Wang, F. Pan, Q. Zhao, M. Lv and B. Zhang, *Front. Chem.*, 2022, **10**, 1055649.
38 Y. An, S. Tan, Y. Liu, K. Zhu, L. Hu, Y. Rong and Q. An, *Energy Storage Mater.*, 2021, **41**, 354–379.
39 B. Hu, J. Xu, Z. Fan, C. Xu, S. Han, J. Zhang, L. Ma, B. Ding, Z. Zhuang, Q. Kang and X. Zhang, *Adv. Energy Mater.*, 2023, **13**, 2203540.
40 T. Huang, G. Zhang, R. Chen, S. Lin, H. Zhou, J. Li, L.-H. Chung, X. Hu, L. Yu and J. He, *ACS Appl. Mater. Interfaces*, 2023, **15**, 21075–21085.
41 K. Sun, C. Wang, Y. Dong, P. Guo, P. Cheng, Y. Fu, D. Liu, D. He, S. Das and Y. Negishi, *ACS Appl. Mater. Interfaces*, 2022, **14**, 4079–4090.
42 A. Zhu, S. Li, Y. Yang, B. Peng, Y. Cheng, Q. Kang, Z. Zhuang, L. Ma and J. Xu, *Small*, 2024, **20**, 2305494.
43 Y. Cao, H. Wu, G. Li, C. Liu, L. Cao, Y. Zhang, W. Bao, H. Wang, Y. Yao, S. Liu, F. Pan, Z. Jiang and J. Sun, *Nano Lett.*, 2021, **21**, 2997–3006.
44 J. Xu, S. An, X. Song, Y. Cao, N. Wang, X. Qiu, Y. Zhang, J. Chen, X. Duan, J. Huang, W. Li and Y. Wang, *Adv. Mater.*, 2021, **33**, 2105178.
45 M. Najafi, S. Bellani, V. Galli, M. I. Zappia, A. Bagheri, M. Safarpour, H. Beydaghi, M. Eredia, L. Pasquale, R. Carzino, S. Lauciello, J.-K. Panda, R. Brescia, L. Gabatel, V. Pellegrini and F. Bonaccorso, *Electrochem*, 2022, **3**, 463–478.
46 V. Marangon, E. Barcaro, L. Minnetti, W. Brehm, F. Bonaccorso, V. Pellegrini and J. Hassoun, *Nano Res.*, 2023, **16**, 8433–8447.
47 Q. Hao, Z.-J. Li, B. Bai, X. Zhang, Y.-W. Zhong, L.-J. Wan and D. Wang, *Angew. Chem., Int. Ed.*, 2021, **60**, 12498–12503.
48 M. Rogojerov, B. Jordanov and G. Keresztury, *J. Mol. Struct.*, 2000, **550–551**, 455–465.
49 L. He, B. Li, Z. Ma, L. Chen, S. Gong, M. Zhang, Y. Bai, Q. Guo, F. Wu, F. Zhao, J. Li, D. Zhang, D. Sheng, X. Dai, L. Chen, J. Shu, Z. Chai and S. Wang, *Sci. China: Chem.*, 2023, **66**, 783–790.
50 M. Wu, Y. Zhao, R. Zhao, J. Zhu, J. Liu, Y. Zhang, C. Li, Y. Ma, H. Zhang and Y. Chen, *Adv. Funct. Mater.*, 2022, **32**, 2107703.
51 A. J. Greenlee, C. I. Wendell, M. M. Cencer, S. D. Laffoon and J. S. Moore, *Trends Chem.*, 2020, **2**, 1043–1051.
52 X. Huang, Z. Wang, R. Knibbe, B. Luo, S. A. Ahad, D. Sun and L. Wang, *Energy Technol.*, 2019, **7**, 1801001.
53 T. Zhu, Q. Wu, Y. Cao, W. Wang, Y. Li, S. Meng and L. Liu, *Electrochim. Acta*, 2023, **447**, 142145.
54 S. Jiang, X. L. Li, D. Fang, W. Y. Lieu, C. Chen, M. S. Khan, D.-S. Li, B. Tian, Y. Shi and H. Y. Yang, *ACS Appl. Mater. Interfaces*, 2023, **15**, 20064–20074.
55 Q. Xu, K. Zhang, J. Qian, Y. Guo, X. Song, H. Pan, D. Wang and X. Li, *ACS Appl. Energy Mater.*, 2019, **2**, 5793–5798.
56 J. Conder, C. Villevieille, S. Trabesinger, P. Novák, L. Gubler and R. Bouchet, *Electrochim. Acta*, 2017, **255**, 379–390.
57 S. Waluś, C. Barchasz, R. Bouchet and F. Alloin, *Electrochim. Acta*, 2020, **359**, 136944.
58 J. Wang, C. Cui, G. Gao, X. Zhou, J. Wu, H. Yang, Q. Li and G. Wu, *RSC Adv.*, 2015, **5**, 47522–47528.
59 Z. Lin and C. Liang, *J. Mater. Chem. A*, 2015, **3**, 936–958.
60 W. Zhu, A. Paolella, C. S. Kim, D. Liu, Z. Feng, C. Gagnon, J. Trottier, A. Vijh, A. Guerfi, A. Mauger, C. M. Julien, M. Armand and K. Zaghib, *Sustainable Energy Fuels*, 2017, **1**, 737–747.
61 M. Chen, X. Fu, N. D. Taylor, Z. Chen and W.-H. Zhong, *ACS Sustainable Chem. Eng.*, 2019, **7**, 15267–15277.
62 X. Fu, C. Li, Y. Wang, L. Scudiero, J. Liu and W.-H. Zhong, *J. Phys. Chem. Lett.*, 2018, **9**, 2450–2459.
63 D. Xiong, S. Huang, D. Fang, D. Yan, G. Li, Y. Yan, S. Chen, Y. Liu, X. Li, Y. Von Lim, Y. Wang, B. Tian, Y. Shi and H. Y. Yang, *Small*, 2021, **17**, 2007442.
64 Y. Zhang, C. Guo, L. Zhou, X. Yao, Y. Yang, H. Zhuang, Y.-R. Wang, Q. Huang, Y. Chen, S.-L. Li and Y.-Q. Lan, *Small Sci.*, 2023, **3**, 2300056.
65 Y. Cho, E. Lee, K. S. Lee, S. J. Hwang, C. W. Kim, T.-G. Kim, S.-K. Kang, S. Y. Park, K. Yoo and Y. Piao, *Electrochim. Acta*, 2023, **447**, 142134.
66 G. Zhou, H. Tian, Y. Jin, X. Tao, B. Liu, R. Zhang, Z. W. Seh, D. Zhuo, Y. Liu, J. Sun, J. Zhao, C. Zu, D. S. Wu, Q. Zhang and Y. Cui, *Proc. Natl. Acad. Sci. U.S.A.*, 2017, **114**, 840–845.
67 X. Yang, X. Li, K. Adair, H. Zhang and X. Sun, *Electrochem. Energy Rev.*, 2018, **1**, 239–293.
68 H. M. Bilal, K. Yuksel and D. Eroglu, *ChemistrySelect*, 2023, **8**, e202203944.
69 M. J. Klein, K. Goossens, C. W. Bielawski and A. Manthiram, *J. Electrochem. Soc.*, 2016, **163**, A2109.
70 M. Sadd, M. Agostini, S. Xiong and A. Matic, *ChemPhysChem*, 2022, **23**, e202100853.
71 L. Meng, C. Song, Q. Lin, G. Sun, J. Long, X. Zhang, H. Li, J. Hu and S. Ye, *ACS Appl. Mater. Interfaces*, 2023, **15**, 21585–21594.

72 A. Vizintin, M. Lozinšek, R. K. Chellappan, D. Foix, A. Krajnc, G. Mali, G. Drazic, B. Genorio, R. Dedryvère and R. Dominko, *Chem. Mater.*, 2015, **27**, 7070–7081.
73 H. Al Salem, G. Babu, C. V. Rao and L. M. R. Arava, *J. Am. Chem. Soc.*, 2015, **137**, 11542–11545.
74 J. Sun, Y. Sun, M. Pasta, G. Zhou, Y. Li, W. Liu, F. Xiong and Y. Cui, *Adv. Mater.*, 2016, **28**, 9797–9803.
75 C.-X. Bi, L.-P. Hou, Z. Li, M. Zhao, X.-Q. Zhang, B.-Q. Li, Q. Zhang and J.-Q. Huang, *Energy Mater. Adv.*, 2023, **4**, 0010.
76 S. Drvarič Talian, A. Vizintin, J. Moškon, R. Dominko and M. Gaberšček, *J. Electrochem. Soc.*, 2020, **167**, 080526.
77 Y. Song, S. Zhao, Y. Chen, J. Cai, J. Li, Q. Yang, J. Sun and Z. Liu, *ACS Appl. Mater. Interfaces*, 2019, **11**, 5687–5694.
78 H. Liu, X.-B. Cheng, R. Xu, X.-Q. Zhang, C. Yan, J.-Q. Huang and Q. Zhang, *Adv. Energy Mater.*, 2019, **9**, 1902254.
79 P. Guo, K. Sun, X. Shang, D. Liu, Y. Wang, Q. Liu, Y. Fu and D. He, *Small*, 2019, **15**, 1902363.